Two-Dimensional Heterogeneous Model for a Reticulated-Foam Photocatalytic Reactor

Rajnish G. Changrani and Gregory B. Raupp
Dept. of Chemical, Bio & Materials Engineering, Arizona State University, Tempe, AZ 85287

A 2-D heterogeneous convection reaction model for a gas–solid lamp-in-tube annular photocatalytic reactor is presented. The catalyst (TiO_2) is supported on a reticulated-foam monolithic structure placed in the annular space between the UV lamp and the reactor wall. Mass balances for individual species are coupled through the reaction-rate expression that appears in the boundary condition at the fluid–solid interface in heterogeneous catalytic reactor models. The heterogeneous reaction rate is modeled using semiempirical Langmuir-Hinshelwood-Hougen-Watson (LHHW) kinetics with adsorption constants for various species. The local volumetric rate of energy absorption (LVREA) term in the rate expression was computed using a 3-D polychromatic radiation-field model. The overall system of nonlinear partial differential equations was solved using a combination of the Crank-Nicolson method and the globally convergent Newton-Raphson method. The apparent, average quantum yield in the LHHW kinetic rate form is the single adjustable parameter in the model. Isopropanol (IPA) was chosen as the test contaminant to conduct experimental performance measurements for model validation. Model-predicted radial and axial profiles for bulk and surface concentration reveal that the extent to which mass transport influences the operation of a photocatalytic reactor is determined largely by the local magnitude of the LVREA. Similitude in the scale-up of an annular lamp-in-tube heterogeneous photocatalytic reactor is achieved only when the dimensionless radial radiation profile, as well as corresponding magnitudes of a geometric number, the Peclet number, the Stanton number, and the photocatalytic analog of the Damköhler number, are identical.

Introduction

Photocatalytic oxidation (PCO) employs the energy in ultraviolet (UV) radiation to destroy airborne volatile organic contaminants (Dibble, 1989; Dibble and Raupp, 1990, 1992; Peral and Ollis, 1992; Raupp, 1995; Obee and Brown, 1995; Sauer and Ollis, 1996). PCO has been considered for a wide spectrum of applications ranging from maintaining indoor-air quality (IAQ) (Obee and Brown, 1995) to treating the off-gases from an air-stripping or soil-vapor-extraction (SVE) unit (Read et al., 1996).

Although bench-scale, controlled laboratory studies have shown promising results, commercial realization of photocatalytic oxidation has been limited. To be cost competitive with existing thermal destruction systems, photocatalytic reactors will need to operate with high photon-utilization efficiencies. Many prototypical photoreactor configurations have failed to simultaneously address two key interrelated issues that govern photon utilization: the efficient distribution of UV energy throughout the reactor volume, and the efficient distribution of catalyst per unit reactor volume.

A key factor that distinguishes photocatalytic reactors from conventional thermocatalytic reactors is the controlling nature of the UV radiation field. Gradients in UV intensity are inherent in every photocatalytic reactor, and although certain reactor configurations may ameliorate these gradients, the gradients in volume-loaded reactors cannot be eliminated. Therefore one of the biggest challenges in designing a commercial photocatalytic oxidation reactor is to find a suitable configuration that would minimize gradients in UV intensity,

Correspondence concerning this article should be addressed to G. B. Raupp.

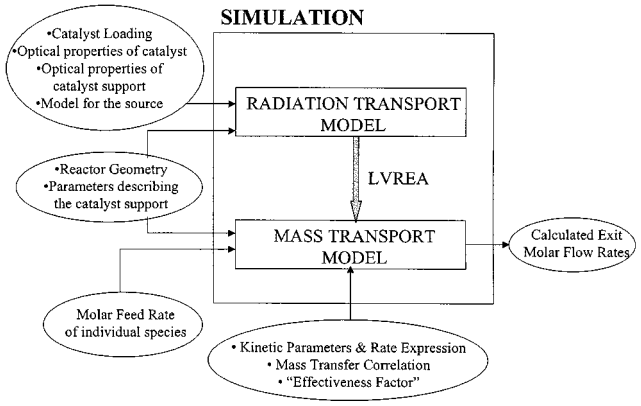

Figure 1. Structure of the reactor simulation showing the key submodels.

and at the same time provide sufficiently large surface area per unit reactor volume, while maintaining low pressure drop operation.

In this article we present the development and validation of a two-dimensional heterogeneous convection-reaction model for an annular reticulated monolithic gas–solid photoreactor. Figure 1 illustrates the interrelationships between the various elements of the reactor model. The radiation field submodel has been recently developed (Changrani and Raupp, 1999), and the data used for parameter extraction and model validation was collected in a series of carefully designed experiments (Changrani and Raupp, 1998).

Experimental

The experimental data used for model validation was collected using a bench-scale PCO system described in detail elsewhere (Raupp et al., 1997). Figure 2 shows the annular geometry of the bench-scale reactor used in the current investigation. A 20-W low-pressure mercury lamp (GE F20T12-BLB) irradiates the reactor from within. The catalyst support is a reticulated-foam monolithic structure, custom fabricated in an annular shape by Hi-Tech Corporation. We have used

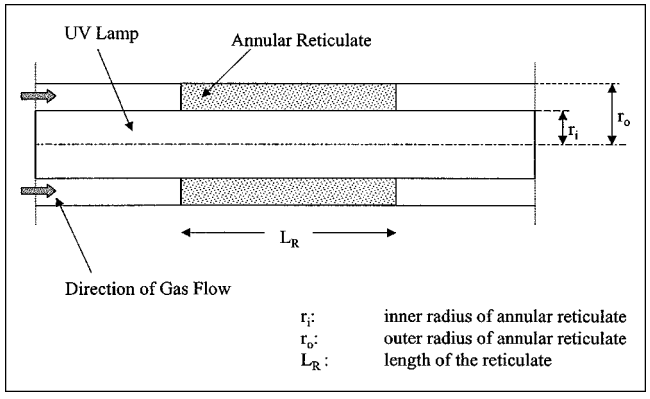

Figure 2. Annular geometry of the bench-scale reactor, showing the reticulate lying along the central portion of the UV lamp.

three alumina reticulates of varying pore-size distribution, classified by the manufacturer as 10 ppi (pores/inch), 20 ppi, and 30 ppi. Quantitative parameters describing the pore-size distribution of individual reticulates have been provided in a recent publication (Changrani and Raupp, 1998).

The alumina reticulates were dip-coated in a slurry of TiO_2 (DeGussa P25) in deionized distilled water (20 g of TiO_2 per liter of water), and then heated in an atmospheric pressure oven at 110°C for 3 h to completely evaporate the water. The catalyst loading on each reticulate was calculated by measuring the change in weight before and after the coating procedure. Light-intensity measurements were made for the uncoated as well as the coated reticulates using an integrating photometer (Minolta). The light intensity was measured at two points designated as r_i and r_o in Figure 2.

In addition to the pore-size distribution and the catalyst loading, the following three independent process parameters were varied on a one-factor-at-a-time (OFA) basis: inlet isopropyl alcohol (IPA) concentration, incident UV intensity, and volumetric flow rate. Details regarding the experimental design matrix have been provided elsewhere (Changrani and Raupp, 1998).

Model Development

Radiation-field model predictions as well as experimental measurements of light absorption in the reticulate consistently indicate the presence of steep radial gradients in the local volumetric rate of energy absorption (LVREA) (Changrani and Raupp, 1999). Existence of these gradients suggests that the portion of the reactor at small radial distances where the LVREA is highest may operate under the influence of mass transport, whereas the regions of the reactor with substantially lower LVREA operate under kinetic control. We therefore chose a heterogeneous model structure to explicitly account for the presence of a separate solid phase and to distinguish between conditions in the bulk fluid and on the solid surface (Froment and Bischoff, 1979).

Two-dimensional heterogeneous convection-reaction model

Model Assumptions.

1. Steady-state operation
2. Isothermal and isobaric operation
3. Angular symmetry, that is, no concentration gradients in the angular direction
4. Plug flow: fully developed axial uniform velocities for all z; negligible radial and angular flow
5. Axial dispersion is negligible
6. Uniform catalyst film thickness
7. Uniform effectiveness factor
8. Negligible thermal reactions
9. Negligible heat of reaction (dilute reactants)
10. Negligible volume change associated with reaction (dilute reactants)
11. Low and constant gas density.

Assumption 2 is justified by experimental measurements. Actual pressure drops were on the order of 0.5 psi across the entire range of experimental flow rates. Assumption 3 is justified by the outcome of the radiation field model, which clearly revealed that LVREA gradients in the angular direc-

tion are absent (Changrani and Raupp, 1999). Assumption 5 is justified when the coefficients of the axial dispersion term in the species mass balance is much smaller than the coefficients of the remaining terms. Calculations for our nondimensionalized system of model equations revealed that the axial dispersion coefficient varied from 10^{-4} to 10^{-3}, and the radial dispersion coefficient varied from 0.1 to 1.0 over the entire range of experimental flow rates. Additional calculations based upon the criteria developed by Mears (1971) revealed that axial dispersion is negligible across the entire range of flow rates and fractional conversions studied in this investigation.

Using these assumptions, the following set of nondimensionalized equations were derived:

$$\frac{\partial \Psi_{jB}}{\partial \lambda} - \frac{1}{Ge \cdot Pe_{mrj}}\left[\frac{\partial^2 \Psi_{jB}}{\partial \xi^2} + \frac{1}{\xi}\frac{\partial \Psi_{jB}}{\partial \xi}\right] + St \cdot \left(\Psi_{jB} - \Psi_{jS}\right) = 0 \tag{1}$$

$$\left(\Psi_{jB} - \Psi_{jS}\right) = \frac{-\sum_{n=1}^{2} \nu_{jn}\eta \hat{R}_n}{k_g a_v C_1^0}, \tag{2}$$

with boundary conditions

$$\begin{aligned} &\Psi_{jB} = 1 && \text{for } j = 1 && \text{at } \lambda = 0 \\ &\Psi_{jB} = 0 && \text{for } j \neq 1 && \text{at } \lambda = 0 \\ &\frac{\partial \Psi_{jB}}{\partial \xi} = 0 && && \text{at } \xi = \xi_t \\ &\frac{\partial \Psi_{jB}}{\partial \xi} = 0 && && \text{at } \xi = \xi_o, \end{aligned} \tag{3}$$

where $\xi = r/(r_o - r_i)$ is the dimensionless radial distance ($2.3 \leq \xi \leq 3.3$); $\xi_i = \xi|_{r=r_i}$ is the dimensionless inner radius; $\xi_o = \xi|_{r=r_o}$ is the dimensionless outer radius; $\lambda = (z/L_R)$ is the dimensionless axial distance; L_R is the reactor length (cm); $\Psi_{jB} = (C_{jB}/C_1^0)$ is the dimensionless bulk concentration of species j; $\Psi_{jS} = (C_{jS}/C_1^0)$ is the dimensionless surface (pore mouth) concentration of species j; C_1^0 is the inlet concentration of IPA (mol·cm^{-3}); $Pe_{mr_j} = (u_s(r_o - r_i)/\epsilon D_{er_j})$ is the radial mass Peclet number for species j; u_s is the superficial velocity (cm/s); ϵ is the void fraction of the reticulate; D_{er_j} is the effective radial diffusivity of the species j (cm^2/s); $Ge = L_R/(r_o - r_i)$ is a dimensionless geometrical ratio; $St = (k_g a_v L_R)/u_s$ is the dimensionless Stanton number; k_g is the gas-phase mass-transfer coefficient (cm/s); a_V is the external surface area per unit reactor volume (cm^2/cm^3); ν_{jn} is the stoichiometric coefficient of the jth species in the nth reaction; η is the effectiveness factor; $\hat{R}_n$ is the intrinsic rate of the nth photoreaction (mol/cm^3·s). Equation 1 is the two-dimensional species mass accounting statement incorporating radial diffusion in the bulk fluid phase and mass transport through an interphase region. Equation 2 equates this local interphase mass transport rate to the photocatalytic reaction rate.

Calculation of the effectiveness factor

Because the thickness of the deposited catalyst film at any point in the reticulated-foam structure is small compared to its principal radius of curvature, we can validly treat the film as having a slab geometry for purposes of estimating effectiveness factors. The effectiveness factors for photocatalytic reactions in porous titania films have been computed for the thin-film (slab) geometry (Edwards et al., 1996) for reactions of order 0, 1, 2 and for reactions following Langmuir-Hinshelwood-Hougen-Watson (LHHW) kinetics. The general Thiele modulus (Λ) and the optical film thickness (Δ) are given by Edwards et al. (1996) as

$$\Lambda^2 \equiv \frac{2L^2 r_0}{DC_{js}\bar{r}} \tag{4}$$

$$\Delta \equiv \mu L, \tag{5}$$

where L is the average length of a pore, r_0 is the reaction rate per unit area evaluated at the surface of the catalyst, D is the reactant diffusion coefficient, C_{jS} is the concentration of the reactant at the pore mouth, $\bar{r}$ is the average pore radius, and μ is the UV light-extinction coefficient. For purposes of computing effectiveness factor values we have employed the value of film thickness for L, the diffusion coefficient D was set equal to a nominal value of 0.1 cm^2/s, the extinction coefficient μ was set equal to 0.3 μm^{-1} (Formenti et al., 1971), and the average pore radius $\bar{r}$ was set equal to 10 nm. We employed globally averaged values for r_0 and C_{jS}; this simplification provides a reasonable estimate of the ratio r_0/C_{jS}. Typical values for the Thiele modulus were on the order of 0.15, and the mean value for optical film thickness (for all three reticulates and different catalyst loading) was 0.9. Based on these values and assuming that the rate expression is similar in mathematical form to a LHHW rate expression for a single site mechanism, the effectiveness factor obtained from the graph provided by Edwards et al. (1996) is approximately 0.7. In this operating regime, the effectiveness factor is only moderately sensitive ($\approx 1/6$) to Thiele modulus, and use of a single effectiveness factor induces only modest errors in the calculations.

Model for the reaction rate

In the photodegradation of IPA we observe acetone and carbon dioxide as the principal gas-phase products (Ameen et al., 1997). Based on this observation, we propose the following sequential reaction scheme:

$$\text{IPA} \rightarrow \text{Acetone} \rightarrow \text{CO}_2.$$

In this scheme we assume that none of the IPA degrades *directly* to carbon dioxide.

Accurate reactor-model predictions require reaction rate expressions valid over the entire range of local conditions, including reactant/product and water-vapor concentrations and the LVREA. Unfortunately, rate expressions that successfully model observed reaction rate shifts as a function of local UV intensity and concentrations have yet to appear in the literature. Instead, empirical or semiempirical expres-

sions that employ a single power-law dependence on UV intensity are typically reported. Because of this limitation, we adopt the following semiempirical LHHW kinetic rate form for a single site mechanism:

$$\hat{R}_j = \left(\Phi_j \cdot \mathrm{LVREA} \left(\frac{K_j C_{jS}}{1 + K_W C_W + \sum_{i=1}^{2} K_i C_{iS}} \right) \right) \qquad (6)$$

where $j = 1, 2$ is the species number (IPA: $j = 1$; acetone: $j = 2$); $\hat{R}_j$ is the intrinsic volumetric rate of photoreaction of species j (mol/cm^3·s); Φ_j is the apparent quantum yield of species j (mol of species j destroyed/mol of photon absorbed); LVREA is local volumetric rate of energy absorption (mol of photon absorbed/cm^3·s); K_j is the equilibrium adsorption parameter for species j (cm^3/mol); C_{jS} is the concentration of species j at the pore mouth (mol/cm^3); K_W is the equilibrium adsorption parameter for water (cm^3/mol); C_W is the concentration of water (mol/cm^3). The first term in the parentheses lumps the complex photocatalytic initiation steps together. The LVREA is determined using the radiation-field submodel, and Φ_j is the single adjustable parameter in this model. The term $K_W C_W$ in the denominator accounts for the typically observed inhibition of the photocatalytic oxidation rate by the presence of water vapor (Dibble, 1989; Dibble and Raupp, 1990; Peral and Ollis, 1992; Junio and Raupp, 1993). In the current investigation we held the relative humidity constant at $\approx 25\%$ RH, corresponding to a water-vapor concentration of 13,000 ppm_V. Because the concentration of IPA as well as acetone was less than 75 ppm_V in all our experiments, we can assume that the relative change in water-vapor concentration was insignificant during the course of the reaction. Therefore, the $K_W C_W$ term was treated as a constant in the present simulations.

Adsorption constants for IPA (K_1), acetone (K_2), and water (K_W) were extracted from in-house experimental data (Ameen et al., 1997). Table 1 summarizes the values of this adjusted parameter Φ_j; these fitted-parameter quantum yields depend upon the reaction conditions.

Mass-transfer correlation

In our experimental VOC conversion tests, the Reynolds number ranged from 0.65 to 9.75, and the characteristic length (mean pore diameter of the reticulated ceramic) ranged from 0.75 mm for the 30-ppi reticulate to 1.5 mm for the 10-ppi reticulate (Hi-Tech Ceramics, Inc.). Bulk mass transfer in this window of process conditions can be approximately represented by (Wakao and Tanisho, 1974)

$$Sh \approx 0.07 Re_p \qquad (7)$$

where Sh is the Sherwood number and Re_p is the Reynolds number based on the mean pore diameter. The diffusivity data required to compute the mass-transfer coefficient from the Sherwood number was obtained for each component using the Chapman-Enskog multicomponent diffusivity equation (Reid et al., 1977).

Table 1. Quantum Yields of IPA and Acetone

Reaction Conditions	Φ_{IPA}	Φ_{ACETONE}
High inlet IPA concentration Low incident UV intensity	1.69	4.63
High inlet IPA concentration High incident UV intensity	1.48	2.99
Low inlet IPA concentration High incident UV intensity	1.32	2.38

Dimensional analysis

For clarity, assume that a single photocatalytic reaction occurs, and that the reaction rate expression reduces to a pseudo-first-order form. For this simplified case, we can rewrite Eqs. 1 and 2 as

$$\frac{\partial \Psi_{jB}}{\partial \lambda} = \frac{1}{N_{Ge} \cdot N_{Pe}} \left[\frac{\partial^2 \Psi_{jB}}{\partial \xi^2} + \frac{1}{\xi} \frac{\partial \Psi_{jB}}{\partial \xi} \right] - N_{St} \cdot \left(\Psi_{jB} - \Psi_{jS} \right) \qquad (8)$$

$$\left(\Psi_{jB} - \Psi_{jS} \right) = \left\{ \frac{\eta \Phi \, \mathrm{LVREA}_0}{k_g a_v} \right\} \cdot \Lambda(\xi) \cdot \Psi_{jS} = N_{Da} \cdot \Lambda(\xi) \cdot \Psi_{jS}, \qquad (9)$$

where N_{Ge} is the geometric number (same as Ge in Eq. 1); N_{Pe} is the Peclet number (same as Pe_{mr_j} in Eq. 1); N_{St} is the Stanton number (same as St in Eq. 1); N_{Da} is the photocatalytic reaction analog of the Damköhler number; LVREA_0 is the LVREA evaluated at the inner reactor wall; $\Lambda(\xi)$ is the dimensionless LVREA radial profile (LVREA normalized by LVREA evaluated at the inner reactor wall).

Equation 9 shows that the magnitude of the interfacial concentration gradient depends on the magnitudes of the Damköhler number and the local value of the dimensionless LVREA radial profile. The Damköhler number physically represents a ratio of characteristic rate of photocatalytic reaction of a characteristic rate of mass transfer to the active surface. The interfacial gradient will be most severe for intrinsically fast reactions, catalyst supports and flow conditions that yield inherently slow mass-transfer rates, and high local UV intensities. At a given axial length down the reactor, interfacial gradients will be less severe with increasing annular radius (distance from the UV lamp).

The dimensionless Stanton number N_{St} represents a ratio of the characteristic rate of reactant mass transfer to the active surface to the characteristic rate of reactant flow by convection. For annular photoreactors operating in a regime influenced by mass transport, modification of the catalyst support or/and flow conditions to yield inherently high mass-transfer rates will cause the conversion to increase.

Based on the terms in Eqs. 8 and 9, we conclude that the resulting concentration field (and hence reactant conversion) will take the general form:

$$\Psi = \Psi\left\{ N_{Ge}, N_{Pe}, N_{St}, N_{Da}, \Lambda(\xi) \right\}. \qquad (10)$$

For scale-up of an annular photoreactor similar to the one used in the bench-scale study, the corresponding dimensionless groups in Eq. 10 as well as the dimensionless radial radiation profile must have identical values to maintain similitude. These dimensionless groups along with similarity they ensure are expressed in Table 2.

Critical inspection of these groups suggests that accurate scale-up for this reactor configuration in a way other than simply employing multiple identical tubes would be problematic. To ensure geometric similarity for a substantially increased reactor length (and hence volume), the annulus width $(r_o - r_i)$ must be increased. Because commercial UV lamps are available only in standard diameters, beyond a certain size the outer radius will need to be increased while maintaining the inner radius constant. For fixed catalyst support and catalyst characteristics, this increase will result in a significantly different LVREA profile, and a different total volume-averaged rate of energy absorption.

To maintain similarity in the LVREA profile for scaled-up reactor dimensions, a different catalyst support structure would be needed. However, built into the Stanton number is the term $a_v L_R$, which physically represents active catalytic surface area per reactor cross-sectional area; this ratio could change significantly from one support to another. Moreover, the dimensionless group N_{Pe} increases when the annulus width increases. To maintain N_{Pe} constant, the superficial velocity would need to be decreased or/and the voidage ϵ increased. It therefore seems highly unlikely that a different physical structure could simultaneously yield similitude in the LVREA profile, the Stanton number, the Peclet number, and the Damköhler number. From the foregoing discussion it is clear that variations in any geometric/spatial parameter simultaneously affect the catalyst distribution and the UV distribution within the active reactor volume, thus making it difficult to predict the effect of these changes on the photoreactor performance without a validated reactor model.

Numerical solution of the model equations

The species mass balances (Eq. 1) can be classified as nonlinear partial differential equations coupled by the reaction rate expression incorporated in the boundary condition at the fluid–solid interface (Eq. 2). These model equations were numerically solved as follows:

1. At $z = 0$ (reactor inlet) assume the surface concentrations to be a certain fraction of the bulk concentration (this assumption is made *only to initialize* the program and obviously does not affect the final solution). Solve the species mass balances (Eq. 1) for all three components independently—obtain bulk concentrations at every radial point at $z = 0$. Solve the species mass balances independently using the Crank-Nicolson method (Carnahan et al., 1969).

2. Using the computed bulk concentrations, solve the equation for the boundary condition at the fluid–solid interface (Eq. 2) for IPA and acetone simultaneously. The LHHW kinetic rate form causes the boundary condition at the fluid–solid interface to be a nonlinear algebraic equation. Simultaneous solution of nonlinear algebraic equations for the two components was accomplished using a globally convergent Newton's method (Press et al., 1996). Because carbon dioxide does not appear in the rate expression (see Eq. 6), it

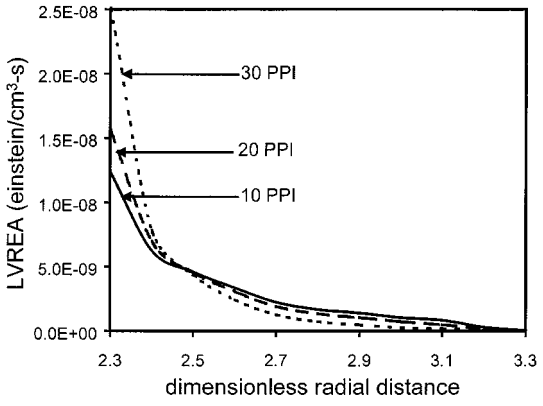

Figure 3. Axial-averaged radial profiles of LVREA in the 10, 20 and 30 ppi reticulate with a nominal catalyst loading.

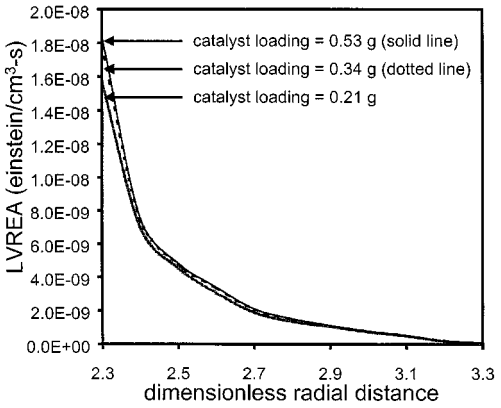

Figure 4. Effect of catalyst loading on the axial-averaged radial profiles of LVREA in the 20 ppi reticulate.

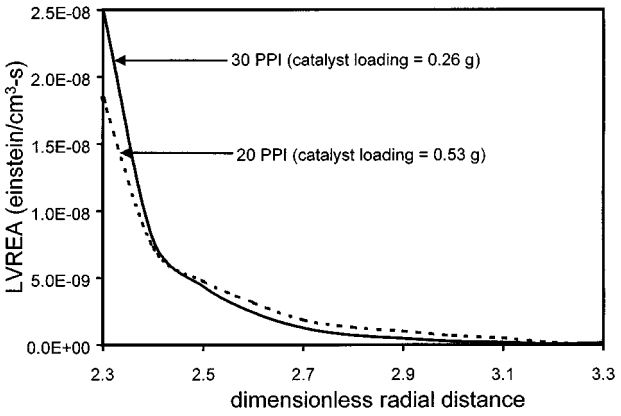

Figure 5. Axial-averaged radial profiles of the local volumetric rate of energy absorption in the 20 ppi reticulate with a high catalyst loading (0.53 g), and the 30 ppi reticulate with a nominal catalyst loading (0.26 g).

was necessary to solve only two nonlinear algebraic equations simultaneously, and the surface concentration of carbon dioxide is obtained by assuming that all the acetone reacts to form carbon dioxide. The solution of the boundary condition at the fluid–solid interface provides new values for surface concentrations at every radial point.

3. Using the new values of surface concentrations, solve the species mass-balance equations independently to obtain new bulk concentrations.

4. Use the new bulk concentrations to compute new surface concentrations as explained in step 2.

5. Iterate between steps 3 and 4 until the species mass balances and the boundary conditions at the fluid–solid interface are satisfied for the same values of bulk and surface concentration—convergence is confirmed at every radial point for a given z.

6. Move ahead in the axial (z) direction. At all subsequent axial points (aside from $z = 0$), the first set of iterations is begun using the surface concentrations from the previous axial point.

7. Decrease the step size in the axial direction and radial direction until the final solution is unchanged. Because the Crank-Nicolson method employed is unconditionally stable, step sizes in the axial and radial direction could be changed independent of each other.

Results and Discussion

The behavior of a photocatalytic reactor can be largely explained in terms of the LVREA within the reactor. Figure 3 shows the radial LVREA profiles in the reticulated-foam photocatalytic reactor as a function of the catalyst support structure, Figure 4 shows the radial LVREA profiles in the reticulated-foam photocatalytic reactor as a function of the catalyst loading, and Figure 5 shows the radial LVREA profiles for the 20 ppi reticulate with a catalyst loading of 0.53 g and the 30 ppi reticulate with a catalyst loading of 0.26 g. We call the LVREAs in Figures 3 to 5 "useful" LVREA, implying that the LVREA is calculated using the photons absorbed by the active catalyst layer and not the photons ab-

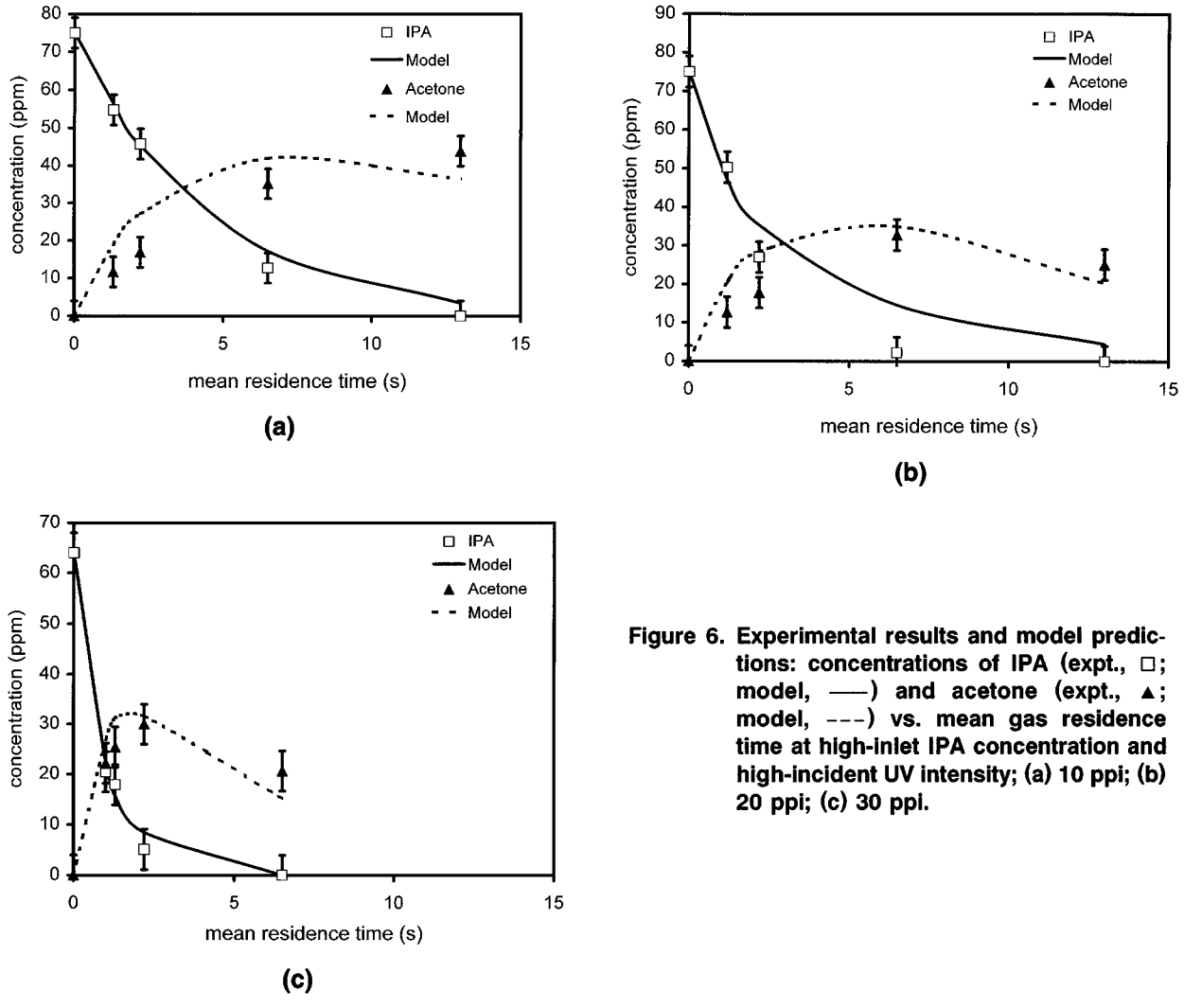

Figure 6. Experimental results and model predictions: concentrations of IPA (expt., □; model, ——) and acetone (expt., ▲; model, – – –) vs. mean gas residence time at high-inlet IPA concentration and high-incident UV intensity; (a) 10 ppi; (b) 20 ppi; (c) 30 ppi.

sorbed by the inert catalyst support. Figures 3 to 5 are obtained for conditions of high incident UV intensity, using a 3-dimensional polychromatic radiation-field model for the reticulated-foam photocatalytic oxidation reactor (Changrani and Raupp, 1999), which has been used as a submodel in the development of the current convection–diffusion–reaction model.

The experimental VOC conversion data along with model-predicted conversions are summarized graphically in Figures 6a–6c to 11a–11c. In all figures, IPA and acetone concentration are plotted vs. mean gas residence time. Figures 6a–6c compare the performance of the three reticulates with similar catalyst loading under experimental conditions of high-inlet IPA concentration and high-incident UV intensity. Figures 7a–7c compare the performance of the three reticulates with similar catalyst loading under experimental conditions of high-inlet IPA concentration and low-incident UV intensity. Figures 8a–8c compare the performance of the three reticulates with similar catalyst loading under experimental conditions of low-inlet IPA concentration and high-incident UV intensity. Figures 9a–9c show the effect of increasing catalyst loading on the 20 ppi reticulate under experimental conditions of high-inlet IPA concentration and high-incident UV intensity. Figures 10a–10c show the effect of increasing catalyst loading on the 20 ppi reticulate under experimental conditions of high-inlet IPA concentration and low-incident UV intensity. Figures 11a–11c show the effect of increasing catalyst loading on the 20 ppi reticulate under experimental conditions of low-inlet IPA concentration and high-incident UV intensity. The qualitative nature of the curves in Figures 6a–6c to 11a–11c are similar to those obtained in a reaction following a series mechanism. The experimental uncertainty was in the range of ± 2 to ± 4 ppm_V for the entire data set of 60 experimental runs.

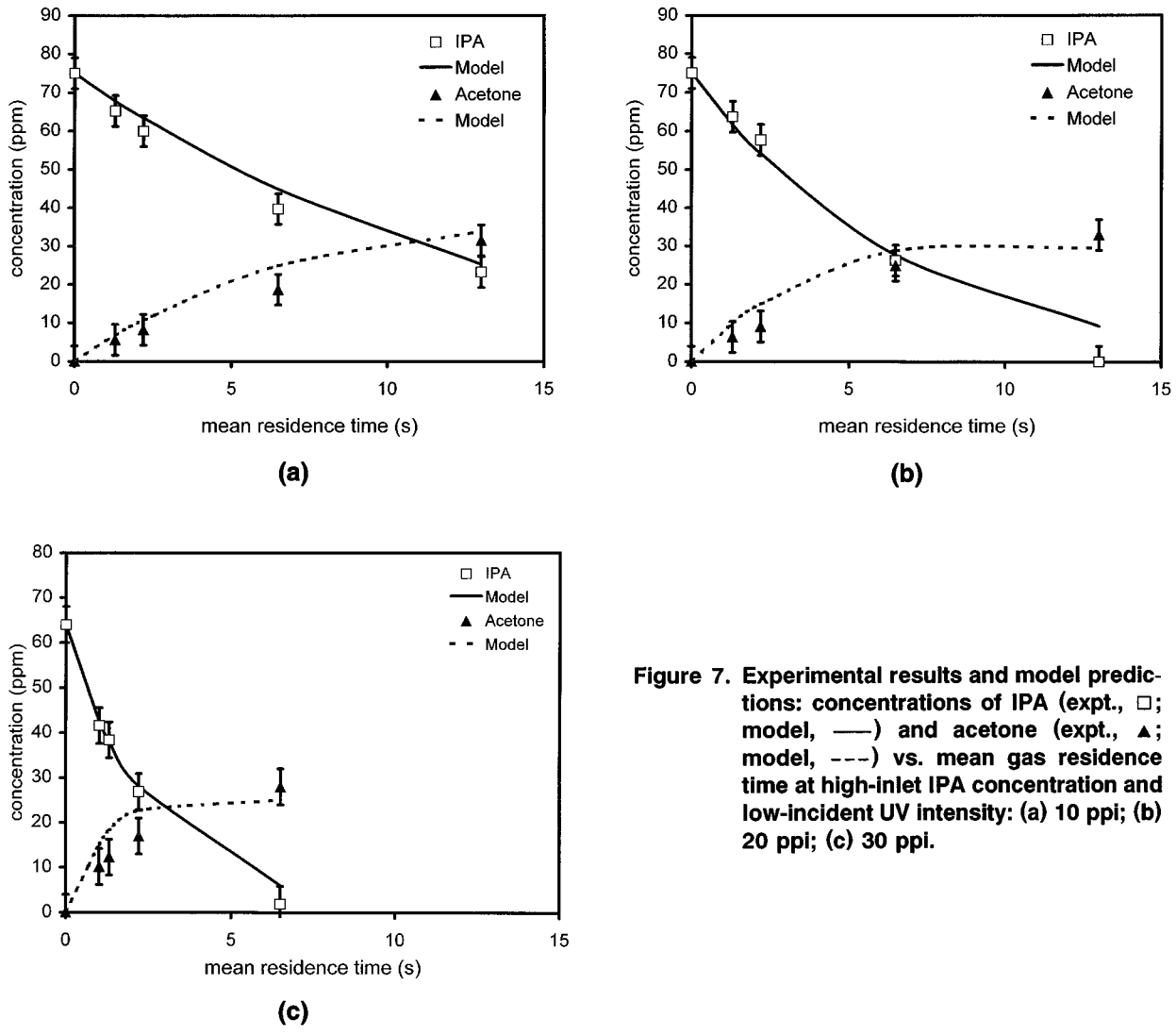

Figure 7. Experimental results and model predictions: concentrations of IPA (expt., □; model, ——) and acetone (expt., ▲; model, – – –) vs. mean gas residence time at high-inlet IPA concentration and low-incident UV intensity: (a) 10 ppi; (b) 20 ppi; (c) 30 ppi.

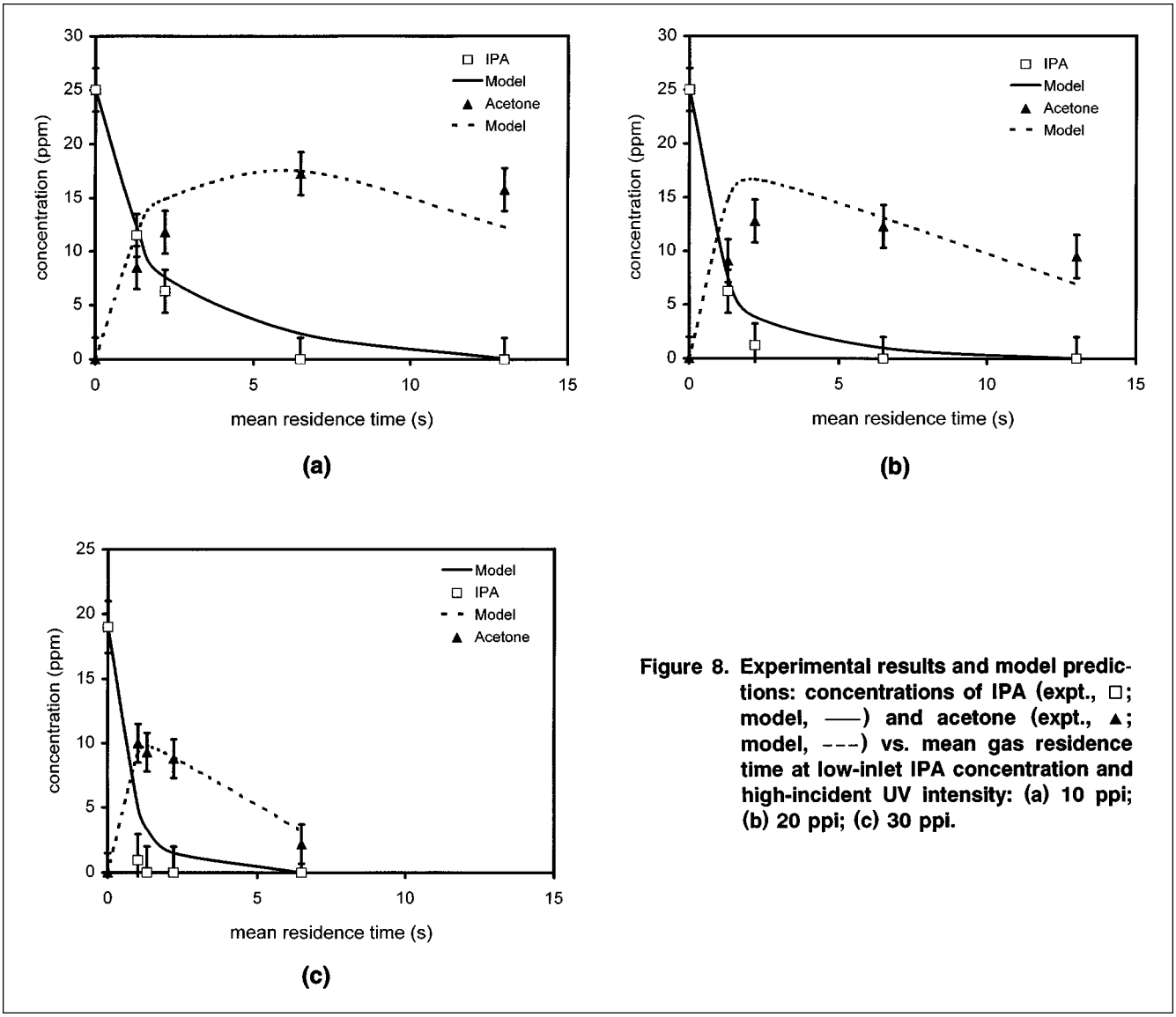

Figure 8. Experimental results and model predictions: concentrations of IPA (expt., □; model, ——) and acetone (expt., ▲; model, – – –) vs. mean gas residence time at low-inlet IPA concentration and high-incident UV intensity: (a) 10 ppi; (b) 20 ppi; (c) 30 ppi.

The quantitative metrics used to compare the performance of the different reticulates are (1) residence time required to achieve 95% IPA degradation, and (2) maximum and final acetone concentrations.

The model-predicted curves shown in Figures 6a–6c to 11a–11c were obtained using a single adjustable parameter–the apparent quantum yield of the organic contaminants. The quantum yields of IPA as well as acetone strongly depend on reaction conditions, but are independent of the characteristics of the reticulated catalyst support. Table 2 summarizes the apparent quantum yields of IPA and acetone for different reaction conditions. The trend followed by the quantum yield of each organic contaminant can be explained by noting that the intrinsic rate of a photoreaction is a function of the local values of concentration and intensity. It has been reported that the rate of photoreaction (or quantum yield) has a nonlinear dependence on light intensity for many degradation reactions (Hoffmann et al., 1995). The nonlinear dependence of the photoreaction rate on intensity is attributed to increased carrier recombination at higher light intensities (Hoffmann et al., 1995).

At experimental conditions of high-inlet VOC concentration and low UV intensity, the local values of concentration at an arbitrary point in the reactor are large enough to efficiently utilize the generated electron–hole pairs and in turn prevent recombination. We therefore observe higher values for the quantum yields of IPA as well as acetone under these conditions. At experimental conditions of high-inlet VOC concentration and high UV intensity, the local values of concentration at an arbitrary point in the reactor are not large enough to efficiently utilize the increased number of electron-hole pairs generated at conditions of high intensity. It is therefore plausible that significant electron–hole recombination occurs, leading to lower values for the quantum yields of IPA as well as acetone. Finally, for experimental conditions of low-inlet VOC concentration and high UV intensity, the

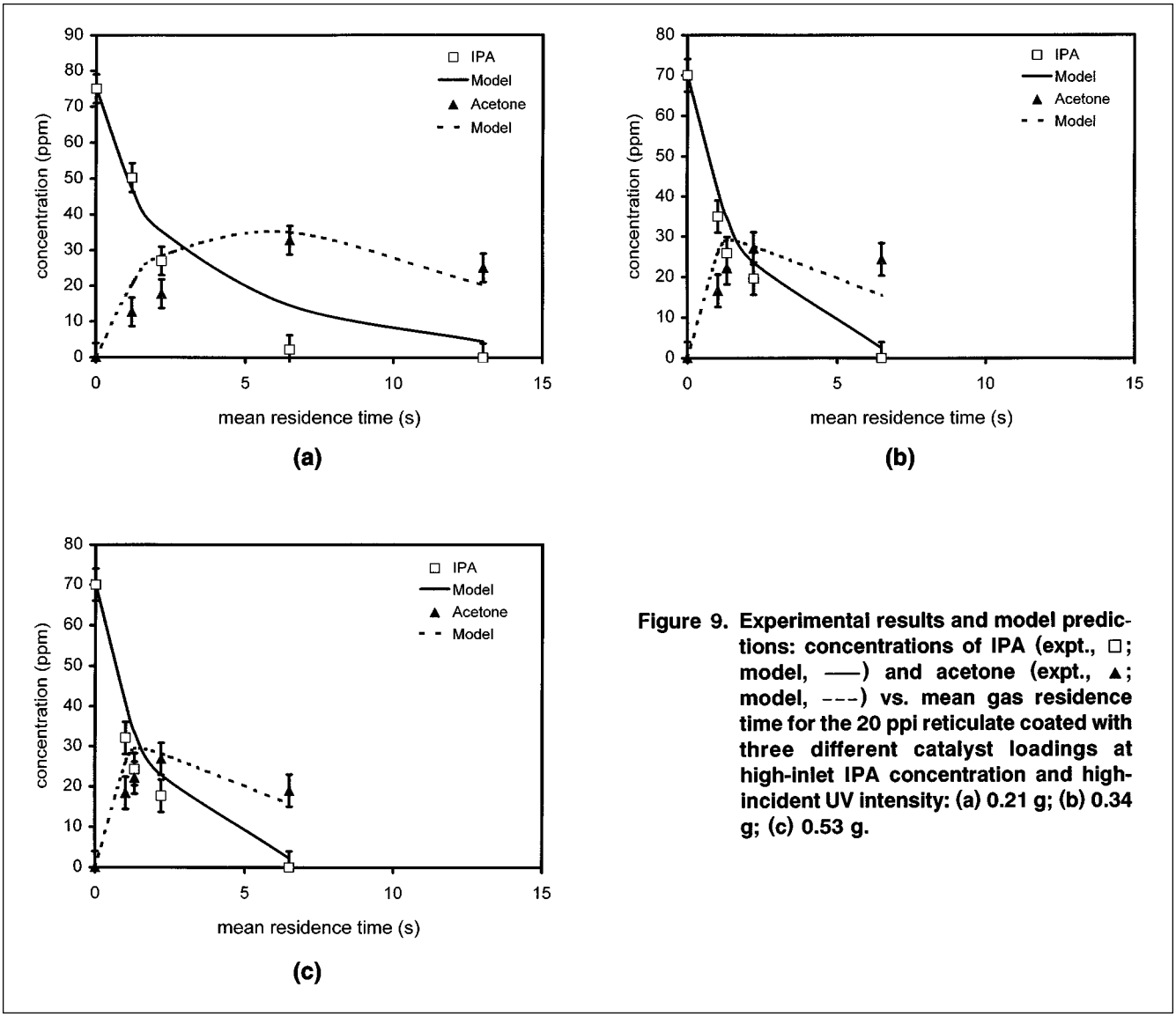

Figure 9. Experimental results and model predictions: concentrations of IPA (expt., □; model, ——) and acetone (expt., ▲; model, – – –) vs. mean gas residence time for the 20 ppi reticulate coated with three different catalyst loadings at high-inlet IPA concentration and high-incident UV intensity: (a) 0.21 g; (b) 0.34 g; (c) 0.53 g.

local values of concentration at an arbitrary point in the reactor are too small to efficiently utilize the large number of electron–hole pairs generated at conditions of high intensity. Therefore a large fraction of the electron–hole pairs undergo recombination, leading to even lower values for the quantum yields of the two organic contaminants.

Before proceeding further with the discussion of these results, it should be noted that in spite of the fact that experimental measurements were made under nominal steady-state conditions where the concentrations of IPA, acetone, and CO_2 were constant, we did not obtain complete carbon mass balance. In selected runs we employed an on-line CO sensor and found varying low levels of carbon monoxide formation, usually on the order of 1–2 ppm_V; we conclude that CO formation is not the cause of mass-balance nonclosure. In a recently conducted set of independent experimental tests, we have verified that potential low molecular-weight partial-oxidation intermediate byproducts such as formaldehyde, acetaldehyde, and formic acid (Ameen, 1998) can be detected by our GC FID. However, during the photodegradation of IPA, acetone was the only intermediate detected by the GC-FID. We conclude that acetone is the only gas-phase intermediate being formed, and that potential C-containing partial-oxidation intermediates accumulate to build up an inventory on the active surface, in spite of the apparent steady levels of gas-phase reactants, intermediates, and products. In a recent *in situ* infrared spectroscopy study, we tentatively identified acetaldehyde, formaldehyde, and formic acid as principal surface intermediates during IPA PCO (Ameen, 1998). In order to confirm that the apparent steady levels of gas-phase reactants, intermediates, and products we observed during a 4-h experimental run is the actual steady state, and to check for catalyst deactivation, we ran selected experiments over a period of five days. We did not observe any changes in the levels of the gas-phase reactants, intermediates, or products after the first few hours of operation. We

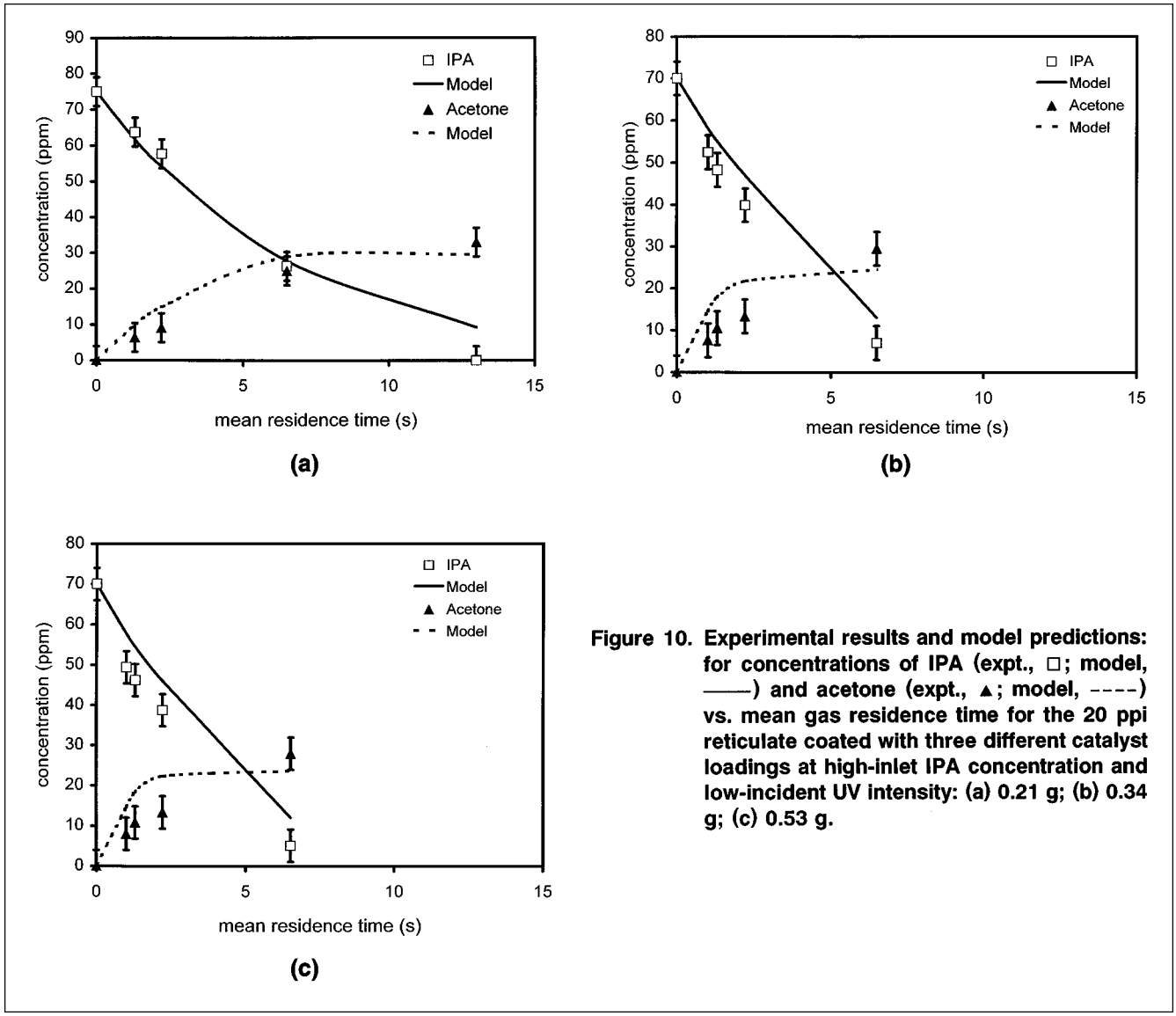

Figure 10. Experimental results and model predictions: for concentrations of IPA (expt., □; model, ——) and acetone (expt., ▲; model, ----) vs. mean gas residence time for the 20 ppi reticulate coated with three different catalyst loadings at high-inlet IPA concentration and low-incident UV intensity: (a) 0.21 g; (b) 0.34 g; (c) 0.53 g.

therefore concluded that there is no catalyst deactivation, and that the lack of mass-balance closure is due to an accumulation of nonpoisoning C-containing partial-oxidation intermediates on the surface. Sauer and Ollis (1996) have reported mass-balance difficulties in alcohol photocatalytic oxidation over a coated ceramic monolith in a batch-recirculating system at low conversion times. Eventually all carbon was recovered as carbon dioxide. The authors attributed this temporary carbon deficit to reversible adsorption of intermediates on ''dark'' surfaces that were not effectively irradiated.

We have modeled the complete photocatalytic oxidation of IPA as a sequential reaction. Since acetone is the only reaction intermediate for which experimental data were available, the model did not incorporate any additional intermediates that may be formed. Model-predicted carbon dioxide concentrations are much higher than experimentally observed carbon dioxide concentrations, because theoretically (that is, in the model) we obtain complete mass-balance closure with all the acetone reacting to form CO_2. Figures 6a–6c to 11a–11c therefore contain information on the reactant (IPA), and only the single intermediate (acetone) that was experimentally observed.

Effect of catalyst support structure

Figures 6a–6c, 7a–7c, and 8a–8c show that the 30 ppi reticulate outperforms the 20 ppi reticulate, and although the 20 ppi reticulate outperforms the 10 ppi reticulate, the performance difference between these two reticulates is not as large. These performance differences can be explained largely in terms of the LVREA profiles represented in Figure 3. Figure 3 reveals that the 30 ppi reticulate captures significantly more of the incident UV energy than either the 20 or the 10 ppi reticulates with similar catalyst loading, with the difference between the light captured by the 20 ppi and the 10 ppi reticulates not being as large. The available specific surface

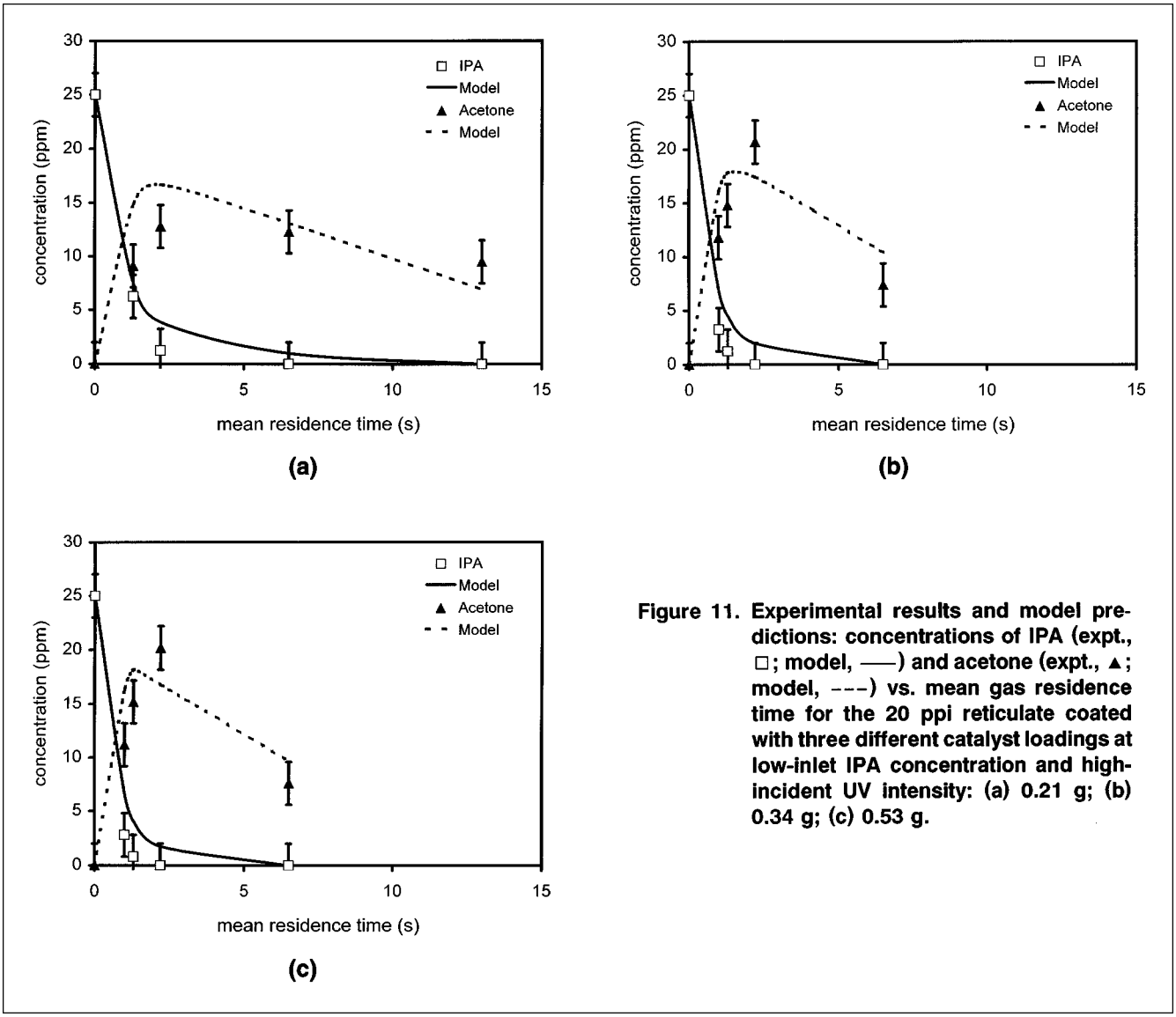

Figure 11. Experimental results and model predictions: concentrations of IPA (expt., □; model, ——) and acetone (expt., ▲; model, – – –) vs. mean gas residence time for the 20 ppi reticulate coated with three different catalyst loadings at low-inlet IPA concentration and high-incident UV intensity: (a) 0.21 g; (b) 0.34 g; (c) 0.53 g.

area per unit reactor volume is a second factor that contributes to the observed performances. The specific surface area per unit volume (a_V) is 43.7 cm^2/cm^3 for the 30 ppi reticulate, 34.0 cm^2/cm^3 for the 20 ppi reticulate, and 22.9 cm^2/cm^3 for the 10 ppi reticulate (Hi-Tech Corporation, private communication, 1998). Therefore the 30 ppi reticulate, which both provides the highest surface area for gas–solid contact and captures the highest fraction of incident UV radiation, is the most efficient catalyst support structure.

Table 2. Dimensionless Groups

Dimensionless Group	Similarity Ensured
$N_{Ge} = \dfrac{r_o - r_i}{L_R}$	Geometric
$N_{Pe} = \dfrac{(r_o - r_i)u_s}{D_{er}}$	Kinematic
$N_{St} = \dfrac{k_g a_V L_R}{u_s} \equiv k_g a_V \tau$	Gas–solid contact opportunity (τ is the mean residence time)
$N_{Da} = \dfrac{\eta \Phi \, \mathrm{LVREA}_0}{k_g a_V}$	Characteristic reaction rate relative to characteristic mass-transfer rate
$\Lambda(\xi)$	Radiation field

Effect of catalyst loading

Figures 9a–9c, 10a–10c, and 11a–11c show the effect of increasing catalyst loading on the performance of the 20 ppi reticulate for different reaction conditions. Under all experimental conditions, the performance of the 20 ppi reticulate is significantly enhanced as the catalyst loading is first increased by almost 60% (0.21 to 0.34 g). However, increasing the catalyst loading by another 60% (0.34 to 0.53 g) was seen to have only a marginal effect on the reticulate's performance. This observed trend is nearly entirely explained by the radial LVREA profiles as a function of catalyst loading represented in Figure 4. Specifically, as the catalyst loading is

first increased by 60% from the nominal value, the increase in the useful LVREA is slightly greater than 10%, but as the catalyst loading is subsequently increased by another 60%, the increase in the useful LVREA is marginal (approximately 1%).

It is interesting to note that the performance of the 20 ppi reticulate with a catalyst loading of 0.53 g is similar to the performance of the 30 ppi reticulate with a catalyst loading of 0.26 g. This similarity in behavior can be explained entirely in terms of the LVREA profiles represented in Figure 5. Figure 5 reveals that the useful LVREA in the portion of the reticulate near the lamp (small radial distance) is approximately 33% higher for the 30 ppi reticulate relative to that for the 20 ppi reticulate. The rate of decay of the LVREA in the radial direction is higher for the 30 ppi reticulate, however, leading to lower LVREA values than the 20 ppi reticulate for dimensionless distances greater than 2.4. The area under the curves in Figure 5 provide a visual insight into the fraction of energy absorbed by each of the reticulates under consideration. The average LVREA for the 30 ppi reticulate was computed to be 3.3×10^{-9} einstein/cm^3-s, and the average LVREA for the 20 ppi reticulate with a catalyst loading of 0.53 g was computed to be 3.4×10^{-9} einstein/cm^3-s. Another interesting fact revealed by Figure 5 is that, in spite of the fact that the 30 ppi reticulate operates under largely dark conditions ($\xi > 2.8$), the performance of the 30 ppi reticulate is similar to the performance of the 20 ppi reticulate with a catalyst loading 0.53 g. This observation highlights a key advantage of using reticulated monoliths as catalyst support structures in photocatalytic reactors. Specifically, the random web structure of the reticulate enhances gas mixing and decreases the probability of contaminant molecules simply ''bypassing'' entirely through ''dark'' regions of the photoreactor.

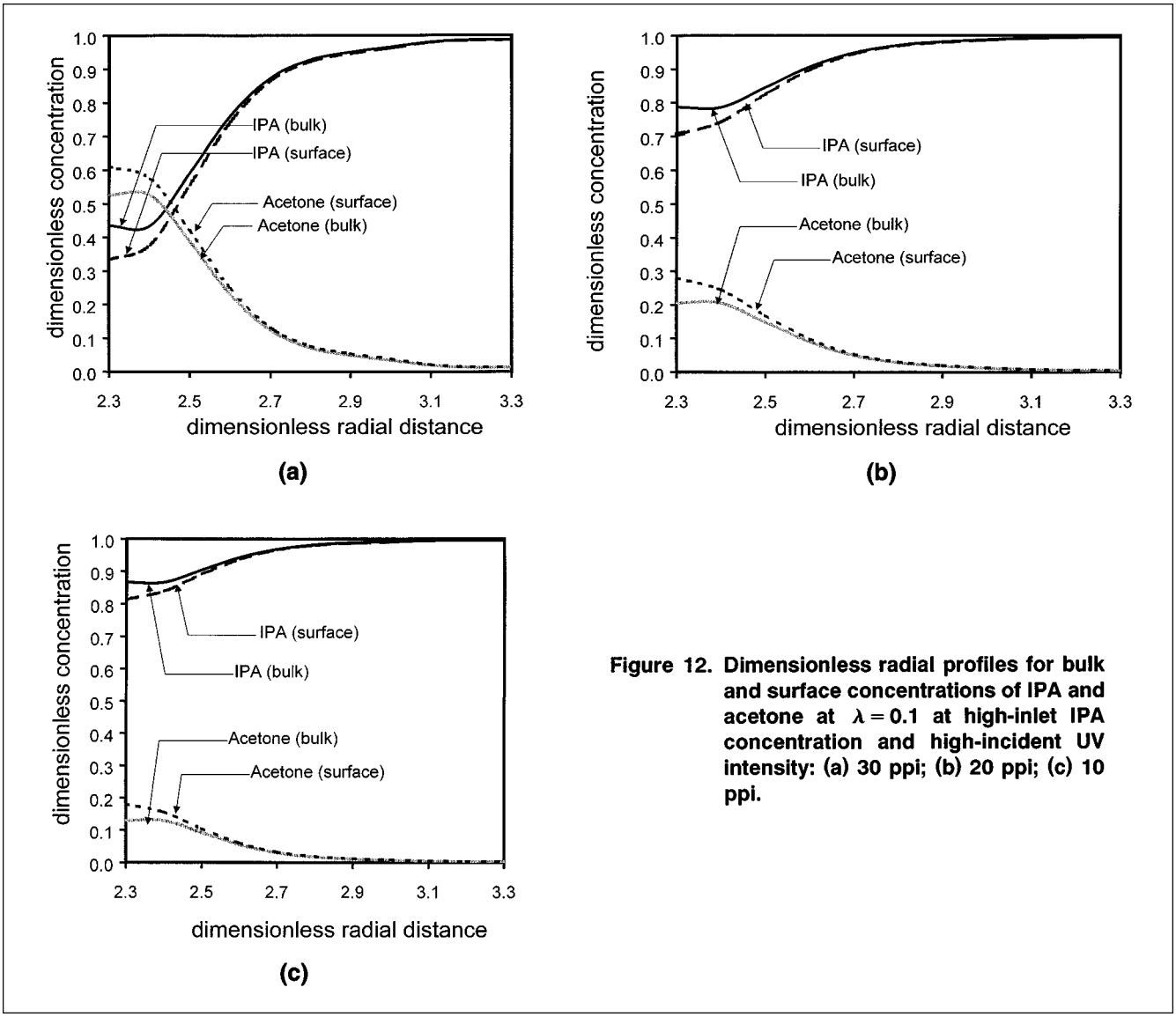

Figure 12. Dimensionless radial profiles for bulk and surface concentrations of IPA and acetone at $\lambda = 0.1$ at high-inlet IPA concentration and high-incident UV intensity: (a) 30 ppi; (b) 20 ppi; (c) 10 ppi.

Influence of mass transport

Figures 12a–12c shows the radial profiles (at $\lambda = 0.1$) for bulk and surface concentrations of IPA and acetone with the 30, 20, and 10 ppi reticulates as the catalyst support, and experimental conditions of high inlet IPA concentratrion and high incident UV intensity. The differences in the bulk- and surface-concentration profiles that exist in the three reticulates are largely explained by the LVREA profiles that exist in these reticulates (see Figure 3). Figure 3 reveals that although the 30 ppi reticulate captures the highest fraction of the incident energy, it does so at the expense of severe radial gradients in the useful LVREA, and consequently significant radial gradients in the intrinsic rate of photoreaction. The intrinsic rate of photoreaction is the highest in the portions of the reactor near the lamp (small radial distance), contributing to the observed difference between the bulk and surface concentration of IPA and acetone in Figure 12a. In contrast, the 10 ppi reticulate captures the smallest fraction of the incident energy, induces the smallest radial gradient in the useful LVREA, and consequently a small radial gradient in the intrinsic rate of photoreaction, which explains the small difference between bulk and surface concentrations of IPA and acetone seen in Figure 12c. The radial profiles for the 20 ppi reticulate represented in Figure 12b are midway between the 10 and the 30 ppi reticulates.

Figure 13 shows the axial profile for bulk and surface concentrations of IPA and acetone at different dimensionless radial distances in the reactor, with the 30 ppi reticulate as the catalyst support and conditions of high-inlet IPA concentration and high-incident UV intensity. Figure 14 shows the axial profile for the *difference* between the bulk and surface concentrations of IPA and acetone at different dimensionless radial distances in the reactor, with the 30 ppi reticulate as the catalyst support and conditions of high-inlet IPA concentration and high-incident UV intensity.

Mass transport influences reactor performance at high intrinsic rates of reaction. In photocatalytic reactors high concentrations and high LVREAs promote high intrinsic rates.

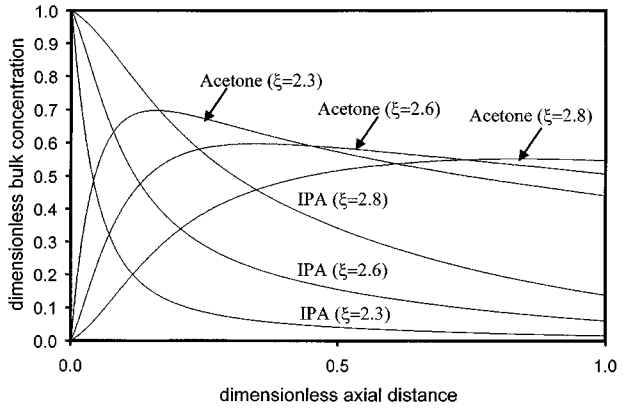

Figure 13. Dimensionless axial profile for bulk concentrations of IPA and acetone at three different points along the annulus width $\xi = 2.3$, $\xi = 2.6$, and $\xi = 2.8$, with 30 ppi reticulate as a catalyst support at high-inlet IPA concentration and high-incident UV intensity.

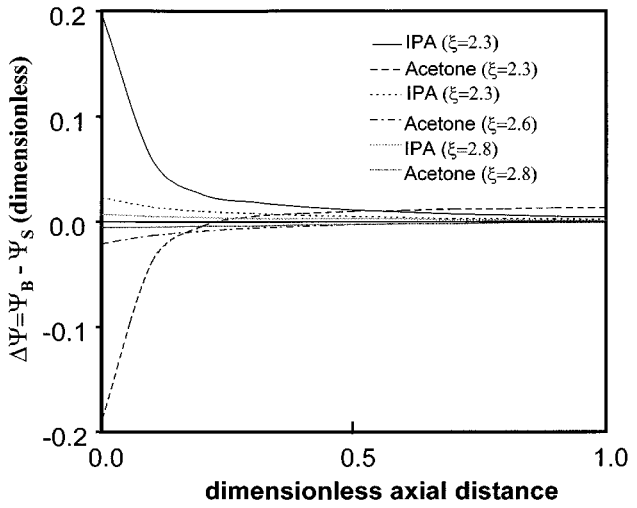

Figure 14. Dimensionless axial profile for the *difference* between bulk and surface concentrations of IPA and acetone at three different points along the annulus width $\xi = 2.3$, $\xi = 2.6$, and $\xi = 2.8$, with 30 ppi reticulate as a catalyst support at high-inlet IPA concentration and high-incident UV intensity.

Because in our experiments we employed only the central portion of the lamp where emission intensity is fairly uniform, we are able to decouple the individual contributions of concentration and LVREA to the mass-transport influences. Figure 14 clearly reveals that in portions of the reactor where the useful LVREA is very high ($\xi = 2.3$), there is a significant difference between the bulk- and surface-concentration profiles along the reactor length. However, in portions of the reactor where the useful LVREA is moderate ($\xi = 2.6$), there is a marginal difference between the bulk and surface concentrations along the reactor length, with the two concentrations being almost identical midway through the annulus width ($\xi = 2.8$). Figures 12a–12c, 13 and 14 when interpreted together bring out the fact that the influence of mass transport on the operation of a photocatalytic reactor is largely determined by the local values of the LVREA, while local values of concentration have little or no effect. This highlights the fact that ideal operating conditions for a commercial photocatalytic reactor would be a uniformly distributed moderate LVREA, which provides sufficiently large rates of photodegradation, while keeping mass-transport influences at a minimum.

Conclusions

We have developed a two-dimensional heterogeneous convection-reaction model to simulate the performance of an annular titania-coated reticulated monolithic reactor. The reactor model uses a semiempirical Langmuir-Hinshelwood-Hougen-Watson (LHHW) kinetic expression, which in turn employs an empirical apparent quantum yield that relates the rate of photon absorption to the rate of contaminant destruction. Within the limits of experimental error, a reasonable agreement was found between the model-predicted and ex-

perimentally observed exit concentrations, using the quantum yield of the contaminant as the only adjustable parameter.

Within the limitations of model assumptions, the local volumetric rate of energy absorption (LVREA) profiles, the total LVREA, and the external surface area per unit reactor volume (a_V) determine the performance of an annular reticulated monolithic photoreactor. These factors are simultaneously determined by the pore-size distribution characteristics of the reticulated catalyst support, and the catalyst loading. Therefore in the design of photocatalytic reactors employing reticulated monoliths as the catalyst support and key parameter to be optimized is the pore-size distribution of the reticulates, with catalyst loading being large enough to ensure that all of the incident UV energy is captured by the catalyst film.

Commercialization of photocatalytic oxidation will require new concepts in reactor design. The ideal heterogeneous photocatalytic reactor is one that induces marginal gradients in UV intensity while providing sufficiently large LVREAs throughout the reactor volume, provides large external surface area per unit reactor volume, and promotes efficient gas–solid contact, thereby minimizing mass-transport influences. In order to search for configurations that approach the ''ideal,'' it is important to be able to virtually investigate these configurations without having to perform extensive experimental investigations. Our validated reactor model can now be used to investigate alternative reactor configurations and optimize traditional reactor configurations. Virtual explorations such as these will ultimately lead to identification of preferred reactor configurations and catalyst distribution, and provide the necessary engineering scale-up data for full-scale operation.

Acknowledgments

The authors gratefully acknowledge the financial support of the U.S. EPA for the experimental portion of this work. We also thank Dr. Truett Sweeting of Hi-Tech Ceramics for fabricating the custom reticulates to our specifications.

Literature Cited

Ameen, Md. M., ''Kinetics and Mechanisms of the Photocatalytic Oxidation of Dilute Volatile Organic Compounds in Air,'' PhD Diss., Arizona State Univ., Tempe (1998).

Carnahan, B., H. A. Luther, and J. O. Wilkes, *Applied Numerical Methods*, Wiley, New York, p. 451 (1969).

Changrani, R. G., and G. B. Raupp, ''Performance Evaluation of a Titania-Coated Reticulated Foam Photocatalytic Oxidation Reactor,'' *J. Adv. Oxid. Technol.*, **3**, 277 (1998).

Changrani, R. G., and G. B. Raupp, ''Monte Carlo Simulation of the Radiation Field in an Annular Titania-Coated Reticulated Foam Photocatalytic Reactor,'' *AIChE J.*, **45**, 1085 (1999).

Dibble, L. A., ''Gas-Solid Heterogeneous Photocatalytic Oxidation of Trichloroethylene by Near UV-Irradiated Titanium Dioxide,'' PhD Diss., Arizona State Univ., Tempe (1989).

Dibble, L. A., and G. B. Raupp, ''Kinetics of the Gas-Solid Heterogeneous Photocatalytic Oxidation of Trichloroethylene over Near UV-Irradiated Titanium Dioxide,'' *Catal. Lett.*, **4**, 345 (1990).

Dibble, L. A., and G. B. Raupp, ''Fluidized-Bed Photocatalytic Oxidation of Trichloroethylene in Contaminated Air Streams,'' *Environ. Sci. Technol.*, **26**, 492 (1992).

Edwards, M. E., C. M. Villa, C. G. Hill, Jr., and T. W. Chapman, ''Effectiveness Factors for Photocatalytic Reactions Occurring in Planar Membranes,'' *Ind. Eng. Chem. Res.*, **35**, 712 (1996).

Froment, G. F., and K. B. Bischoff, *Chemical Reactor Analysis and Design*, Wiley, New York, p. 546 (1979).

Fromenti, M., F. Juillet, P. Meriadeau, and S. J. Teichner, ''Heterogeneous Photocatalysis for Partial Oxidation of Paraffins,'' *Chem. Technol.*, **1**, 680 (1971).

Hoffmann, M. R., S. T. Martin, W. Choi, and D. W. Bahnemann, ''Environmental Applications of Semiconductor Photocatalysis,'' *Chem. Rev.*, **95**, 69 (1995).

Junio, C. T., and G. B. Raupp, ''Photocatalytic Oxidation of Oxygenated Air Toxics,'' *Appl. Surf. Sci.*, **72**, 321 (1993).

Mears, D., ''Tests for Transport Limitations in Experimental Catalytic Reactors,'' *Ind. Eng. Chem. Process Des. Dev.*, **10**, 541 (1971).

Obee, T. N., and R. T. Brown, ''TiO_2 Photocatalysis for Indoor Air Applications: Effects of Humidity and Trace Contaminant Levels on the Oxidation Rates of Formaldehyde, Toluene, and 1,3-Butadiene,'' *Environ. Sci. Technol.*, **29**, 1223 (1995).

Peral, J., and D. F. Ollis, ''Heterogeneous Photocatalytic Oxidation of Gas-Phase Organics for Air Purification: Acetone, 1-Butanol, Butyraldehyde, Formaldehyde, and m-Xylene Oxidation,'' *J. Catal.*, **136**, 554 (1992).

Press, W. H., S. A. Teukolsky, W. T. Vetterling, and B. F. Flannery, *Numerical Recipes in Fortran 77: The Art of Scientific Computing*, 2nd ed., Cambridge Univ. Press, New York, p. 376 (1996).

Raupp, G. B., ''Photocatalytic Oxidation for Point-of-Use Abatement of Volatile Organic Compounds in Microelectronics Manufacturing,'' *J. Vac. Sci. Technol. B*, **13**, 1883 (1995).

Raupp, G. B., J. A. Nico, S. Annangi, R. G. Changrani, and R. Annapragada, ''Two-Flux Radiation-Field Model for an Annular Packed-Bed Photocatalytic Oxidation Reactor,'' *AIChE J.*, **43**, 792 (1997).

Read, H. W., X. Fu, L. A. Clark, M. A. Anderson, and T. Jarosch, ''Field Trials of a TiO_2 Pellet Based Photocatalytic Reactor for Off-Gas Treatment at a Soil Vapor Extraction Well,'' *J. Soil Contam.*, **5**, 187 (1996).

Reid, R. C., J. M. Prausnitz, and T. K. Sherwood, *The Properties of Gases and Liquids*, 3rd ed., McGraw-Hill, New York, p. 548 (1977).

Sauer, M. L., and D. F. Ollis, ''Photocatalyzed Oxidation of Ethanol and Acetaldehyde in Humidified Air,'' *J. Catal.*, **158**, 570 (1996).

Wakao, N., and S. Tanisho, ''Chromatographic Measurements of Particle-Gas Mass Transfer Coefficients at Low Reynolds Numbers in Packed Beds,'' *Chem. Eng. Sci.*, **29**, 1991 (1974).

Manuscript received June 16, 1999, and revision received Nov. 4, 1999.